

1

Flexible multivariate hemodynamics fMRI data analyses and simulations with PyHRF

Thomas Vincent^{1,2}, Solveig Badillo^{2,3}, Laurent Risser^{2,4}, Lotfi Chaari^{1,5},
Christine Bakhous¹, Florence Forbes¹ and Philippe Ciuciu^{2,3*}

¹INRIA, MISTIS, Grenoble University, LJK, Grenoble, France

²CEA/DSV/I²BM NeuroSpin center, Bât. 145, F-91191 Gif-sur-Yvette, France

³INRIA, Parietal, NeuroSpin center, Bât. 145, F-91191 Gif-sur-Yvette, France

⁴CNRS, Toulouse Mathematics Institute, UMR 5219, Toulouse, France

⁵INP-ENSEEIH / CNRS UMR 5505, University of Toulouse, IRIT, Toulouse, France

Correspondence*:

Philippe Ciuciu

CEA/DSV/I²BM NeuroSpin center, Bât. 145, F-91191 Gif-sur-Yvette, France,
philippe.ciuciu@cea.fr

Research Topic

2 ABSTRACT

3 As part of fMRI data analysis, the `pyhrf` package provides a set of tools for addressing the two
4 main issues involved in intra-subject fMRI data analysis: (i) the localization of cerebral regions
5 that elicit evoked activity and (ii) the estimation of the activation dynamics also referenced to
6 as the recovery of the Hemodynamic Response Function (HRF). To tackle these two problems,
7 `pyhrf` implements the Joint Detection-Estimation framework (JDE) which recovers parcel-level
8 HRFs and embeds an adaptive spatio-temporal regularization scheme of activation maps. With
9 respect to the sole detection issue (i), the classical voxelwise GLM procedure is also available
10 through `nipy`, whereas Finite Impulse Response (FIR) and temporally regularized FIR models
11 are implemented to deal with HRF estimation concerns (ii). Several parcellation tools are also
12 integrated such as spatial and functional clustering. Parcellations may be used for spatial
13 averaging prior to FIR/RFIR analysis or to specify the spatial support of the HRF estimates
14 in the JDE approach. These analysis procedures can be applied either to volumic data sets or
15 to data projected onto the cortical surface. For validation purpose, this package is shipped with
16 artificial and real fMRI data sets, which are used in this paper to compare the outcome of the
17 different available approaches. The artificial fMRI data generator is also described to illustrate
18 how to simulate different activation configurations, HRF shapes or nuisance components. To
19 cope with the high computational needs for inference, `pyhrf` handles distributing computing
20 by exploiting cluster units as well as multiple cores computers. Finally, a dedicated viewer is
21 presented, which handles n -dimensional images and provides suitable features to explore whole
22 brain hemodynamics (time series, maps, ROI mask overlay).

23 **Keywords:** medical imaging analysis, fMRI, Bayesian inference, python, scientific computing

1 INTRODUCTION

24 As Magnetic Resonance Imaging (MRI) is a growing imaging modality in neuroscience, the need
25 for powerful tools to explore the increasing amount of data is more and more significant. This data
26 growth is quantitative as cohort sizes are getting bigger through the development of international multi-
27 centre projects like the Human Brain Project **Koslow and Huerta** (2013) but also qualitative as high
28 field magnets become more and more available **Duyn and Koretsky** (2011). Functional MRI (fMRI)
29 especially benefits from these improvements and the experimenter has access to finer spatial (~ 1 mm)
30 and temporal (~ 1 sec.) resolutions and also higher signal-to-noise ratio (SNR). In particular, the higher
31 temporal resolution combined with higher SNR allows a better recovery of dynamical processes so
32 that we no longer have to accommodate with only static mappings of cerebral activity. In this context,
33 `pyhrf` aims at extracting dynamical features from fMRI data and especially the Blood Oxygenated
34 Level Dependent (BOLD) modality (**Ogawa et al.** (1990)). **The observed BOLD signal is an indirect**
35 **measure of the neural activity via the oxygen variation induced by the neuro-vascular coupling. Therefore,**
36 **analysis methods have to formalize a hemodynamic model in order to make inference on neural processes.**
37 **However, even if BOLD variations are known to correlate with neural activity, it is difficult to disentangle**
38 **the dynamics of neural and the vascular components.** As the employed methodology mainly resorts
39 to linear systems, dynamical processes are summarized within the so-called Hemodynamic Response
40 Function (HRF), which is the impulse response that links neuronal activity to the fMRI signal. In fact, the
41 package offers various tools to analyze evoked fMRI data ranging from spatial mappings such as those
42 provided by the General Linear Model (GLM) framework (**Friston et al.** (1995)) to finer hemodynamics
43 models as provided by the joint detection-estimation (JDE) approach described in **Makni et al.** (2005,
44 2008); **Vincent et al.** (2010). **Through a bilinear and time-invariant system, the JDE approach models an**
45 **unknown HRF at the level of a group of voxels (referred to as a parcel in the following) as well as voxel-**
46 **and condition-specific response levels to encode the local magnitudes of this response. The HRF is only**
47 **constrained to be smooth (temporal regularization) and can cover a wide variety of shapes. The response**
48 **levels are spatially regularized within each parcel. Hence, the JDE approach is a spatially adaptive GLM**
49 **built on unknown parcel-dependent HRFs with spatio-temporal regularization.**

50 The usage of each tool depends on a choice of model which is driven by the features required by the
51 experimenter's questioning. To obtain classical detection results, a GLM based on the canonical HRF (and
52 possibly its temporal derivatives) may be sufficient. Even if the between-region hemodynamics variability
53 is acknowledged, the canonical HRF can provide good results in regions where it has precisely been
54 calibrated such as temporal and occipital cortices as studied by **Boynton et al.** (1996). However, to
55 detect activations in regions involving more complex processes or where potential hemodynamics delays
56 happen (varying reaction delays or pathological cases), hemodynamic fluctuations influencing detection
57 activation may occur that are not caught by the HRF derivatives or function bases. Moreover, if one
58 is interested in studying the dynamics features of the response, an *explicit* HRF estimation is required.
59 The main question in this case concerns the need for condition-specific features or not, namely for an
60 HRF estimation associated with each experimental condition or for a single HRF estimate associated
61 with all conditions. If explicit condition-wise HRFs are required, the best methodological tool to use
62 is the temporally Regularized FIR (RFIR) developed in **Marrelec et al.** (2003); **Ciuciu et al.** (2003).
63 Otherwise, if variability is expected only across separated and specialized regions, the JDE framework is
64 well-suited. Indeed, within a specialized region, if only one condition exhibits activity then the region-
65 specific HRF can be considered a condition-specific HRF. The performance of RFIR models depends
66 nonetheless on the number of experimental conditions involved in the paradigm because the higher this
67 number, the larger the number of parameters to estimate and thus the fewer the number of degrees of
68 freedom for statistical testing. The model choice depends thus also on the experimental paradigm. First, it
69 is worth noticing that the use of the JDE formulation is **less relevant** to analyze block paradigm data since
70 the signal variability in this case is hardly significant. The JDE formalism is actually more adapted to
71 fast event-related paradigms or to paradigms including many conditions, like the localizer paradigm (10
72 conditions) introduced by **Pinel et al.** (2007) and used hereafter in this paper. The JDE approach is also
73 optimally tuned to combined analysis of hemodynamics features with the detection of activated brain

74 areas. To sum up on the model choice, the JDE model provides a fair compromise with the possibility for
75 the user to adapt the model to the studied region.

76 JDE also delivers interesting and complementary results for the sole activation-detection aspect
77 compared with classical GLM. Spatial regularization, which is necessary due to the low SNR in fMRI, is
78 not enforced in the same way between methods. In the GLM, FIR and RFIR cases, there is no embedded
79 spatial regularization within models. Indeed, the data are usually spatially smoothed with a fixed Gaussian
80 kernel as part of preprocessings. In contrast, JDE incorporates spatial correlation through hidden Markov
81 models. The amount of spatial correlation is automatically tuned and also adaptive across brain regions,
82 therefore avoiding any prior invariant smoothing.

83 `pyhrf` is mainly written in python with some C code to cope with computationally demanding parts
84 of algorithms. This python choice has been made possible thanks to the `nipy`¹ project and especially
85 `nibabel`² to handle data reading/writing in the NIFTI format.

86 In terms of package maturity, `pyhrf` is a research tool which has the ambition to target cognitive
87 neuroscientists and clinicians. Efforts are made in terms of user-friendliness and the design is a trade-off
88 between *mutability* which is required by methodological research where specifications change frequently
89 and *usability* where user interfaces should be as stable as possible to ease external non-developer use
90 cases.

91 The rest of the paper is organized as follows. First, methods available in the package are presented,
92 comprising parcellation and detection/estimation analyses. Then, the workflow and design of the `pyhrf`
93 package are detailed which cover the user interface and code snippets for the main analysis treatments,
94 simulation framework, distributed computations and data viewer. Results illustrate the outcome of
95 geometrical and functional parcellations and their impact on detection/estimation treatments. Finally,
96 conclusions are drawn and perspectives for future developments are indicated.

2 METHODS

97 The main fMRI data analysis methods available in `pyhrf` are of two kinds: (i) parcellation tools that
98 segment the brain into disjoint sets of positions and (ii) activation detection/HRF estimation tools that
99 highlight correlations between the input experimental paradigm and variations in the measured fMRI
100 signal. The first kind comprises two spatial parcellation tools: Voronoi-based random parcellation,
101 as reviewed by **Aurenhammer and Klein** (2000) and balanced partitioning, developed in **Elor and**
102 **Bruckstein** (2009). The second kind comprises the GLM introduced in **Friston** (1998), the FIR model
103 described in **Henson et al.** (2000), the RFIR model developed in **Ciuciu et al.** (2003) and the JDE
104 approach presented in **Vincent et al.** (2010); **Risser et al.** (2011). The GLM and FIR GLM procedures
105 are provided by `nipy` while RFIR and JDE are originally implemented in `pyhrf`. For all these methods,
106 we refer to their respective bibliographical references for an extensive presentation of their methodology.
107 Nonetheless, the main aspects of these methods are summarized in what follows with the concern of
108 allowing the comparison between them, especially in terms of model structure and assumptions.

109 After detailing notations, we introduce detection/estimation methods, namely GLM, FIR and RFIR, which
110 require the measured fMRI signal and the timing of the experimental paradigm as input. After setting
111 the generative model common to all detection/estimation methods and a brief comparative overview,
112 each approach is presented in more details. Subsequently, parcellation methods are presented. Spatial
113 parcellation approaches can be applied directly to the input fMRI data and only depend on its geometry.
114 Functional parcellation, which is a clustering of GLM results, is detailed afterwards.

¹ ADDEDwww.nipy.org

² ADDEDwww.nipy.org/nibabel

2.1 NOTATION

115 *Conventions* We denote vectors with bold lower case (e.g., \mathbf{y}) and matrices with bold upper case letters
 116 (e.g., \mathbf{P}). A vector is by convention a column vector. Scalars are denoted with non-bold lower case letters
 117 (e.g., a). The transpose operation is denoted by t . Probability distribution functions (pdf) are denoted
 118 using calligraphic letters (eg, \mathcal{N} and \mathcal{G} for the Gaussian and gamma distributions).

119 *Data geometry* As methods can be applied to data defined in the volume or on the cortical surface, the
 120 generic term “position” will be used in place of “voxel” (volume unit) and “node” (surface mesh unit).
 121 Position indexes are denoted by $j = 1 : J$ to indicate a range between 1 and J . Data are assumed to be
 122 masked to only keep positions within the brain. J is the total number of positions within the functional
 123 mask. In addition, when considering parcellated data, this functional mask is divided into a set of Γ parcels
 124 denoted $\mathbb{P} = \{\mathcal{P}_1, \dots, \mathcal{P}_\gamma, \dots, \mathcal{P}_\Gamma\}$, where \mathcal{P}_γ is the set of $J_\gamma = |\mathcal{P}_\gamma|$ position indexes belonging to parcel
 125 γ .

126 *Functional data* We consider the usual case of evoked fMRI data analysis where the experimental
 127 paradigm comprising M conditions is known. The signal measured at each time of repetition (TR)
 128 is denoted $\mathbf{y}_j = \{y_{j,n}\}_{n=1:N}$ where N is the number of scans. Stimulus timing onsets for a given
 129 experimental condition $m = 1 : M$ are encoded by variable \mathbf{x}^m so that $x_t^m = 1$ if a stimulus occurs
 130 at time t up to a time step Δt , else $x_t^m = 0$. The time step is such that $\Delta t \leq TR$ and depends on the actual
 131 temporal resolution sought by the analysis method.

2.2 DETECTION/ESTIMATION METHODS

For ease of comparison, the presentation of all methods is immersed in the same formalism where the signal is assumed generated by a linear and time-invariant (convolution) system with additive noise. We also consider the usual case of taking into account a position-specific low frequency drift in the data which is a well known fMRI artifact produced by the aliasing of respiratory and cardiac rhythms into the low frequencies as studied in **Yan et al.** (2009). The generic forward model, reads:

$$\mathbf{y}_j = \sum_{m=1}^M \mathbf{X}^m \phi_h^m + \mathbf{P} \ell_j + \mathbf{b}_j, \quad (1)$$

132 where:

- 133 • \mathbf{P} is a fixed orthonormal basis that takes a potential drift and any other nuisance effect (e.g., motion
 134 parameters) into account. The low-frequency drift can classically be either polynomial with an order
 135 up to 5 or cosine with a cut-off of 0.01Hz,
- 136 • ℓ_j are the unknown regression weights associated to \mathbf{P} ,
- 137 • \mathbf{b}_j is the noise component,
- 138 • ϕ_h^m is a “generic” hemodynamic filter of size D . For a typical duration of 25 sec., $D = 25/TR$ for
 139 the GLM and FIR GLM³ approaches, while $D = 25/(TR/4)$ for the RFIR and JDE approaches
 140 considering a typical oversampling factor of 4. In the GLM framework, ϕ_h^m can be fixed to the
 141 canonical HRF or parametric when resorting to function bases and we will note R the number of
 142 unknown parameters. In non-parametric approaches, all HRF coefficients are estimated as in RFIR or
 143 JDE approaches,

³ Over-sampling could be performed in the case of FIR GLM but is not advisable in terms of estimability since some FIR coefficients may be poorly or even not associated with paradigm covariates in matrix \mathbf{X}^m , depending on the paradigm jittering.

- 144 • \mathbf{X}^m is the $N \times D$ stimulus occurrence matrix consisting of the lagged stimulus covariates for the
 145 experimental condition m : $\mathbf{X}^m = [\mathbf{x}_{t_1}^m, \dots, \mathbf{x}_{t_N}^m]^t$ with $\mathbf{x}_{t_n}^m = (x_{t_n-d\Delta t}^m)_{0 \leq d \leq D}^t$,
- 146 • $\sum_{m=1}^M \mathbf{X}^m \phi_h^m$ is hence the summation of all stimulus-induced signal components which are
 147 generated as the convolution between the paradigm encoded in \mathbf{X}^m and the hemodynamic filters
 148 ϕ_h^m .

149 For the sake of simplicity, multiple-run data are not considered here but all implemented methods can
 150 handle such data with a fixed-effect model (same effect size across runs), a homoscedastic noise model
 151 (one noise variance for all runs) and run-specific drift coefficients (see discussion for further extensions).

152 To give a first overview of how this generative model structure is derived in the different approaches,
 153 Table 1 provides a comparison in terms of regularization, number of unknowns and analysis duration.
 154 Embedded spatial regularization is only available in the JDE procedure, while temporal regularization
 155 is available in RFIR and JDE (Table 1 – 1st, 2nd rows). In terms of constraints applied to the HRF
 156 shape (Table 1 – 3rd row), the basis set GLM (BS GLM) is the most constraining and the shape captured
 157 depends on the choice of the function basis. In the FIR, RFIR and JDE cases, any form of HRF shape
 158 can be recovered, provided that they are smooth in the case of RFIR and JDE. On Table 1 – 4th row,
 159 the information on the number of unknowns conveys the level of parsimony of a given model. BS GLM,
 160 FIR and RFIR have increasing model complexity as the number of parameters for the HRF increases. In
 161 contrast, JDE achieves larger parsimony by making the number of unknowns associated with the HRF
 162 dependent on the number of parcels rather than on the number of positions. When computing the ratio
 163 between the number of unknowns and the number of data points for a typical fMRI experiment (Table 1
 164 – 5th row), it appears that JDE is comparable to a GLM with derivatives. The RFIR presents the worst
 165 situation with 3 times more unknowns than data points. In terms of analysis duration (Table 1 – last
 166 row), GLM methods are almost instantaneous as their inference is straightforward. RFIR relies on an
 167 iterative scheme to perform unsupervised estimation of the amount of temporal regularization and is
 168 hence much slower. In addition, the implementation of RFIR is done in pure python with a main loop
 169 over positions which worsen its slow computation speed (~ 30 h. for a whole brain analysis)⁴. Therefore,
 170 this approach is rather limited to the processing of some regions of interest where we expect cerebral
 171 activity instead of whole brain data analysis. The computation speed of JDE is also slow, but to a lesser
 172 extent as results can be obtained overnight (~ 8 h. for a whole brain analysis) on a single processing unit.
 173 All these considerations on speed have to be nuanced with the access to increasing computing power and
 174 distributed computations, as will be seen in section 3.3.

2.2.1 basis set General Linear Model

In any position j of the brain, the **basis set GLM (BS GLM)** allows for some limited hemodynamic fluctuations by modeling the hemodynamic filter function ϕ_h in Eq. (1) as a weighted sum of the fixed canonical HRF denoted \mathbf{h}_c and its first and second order derivative $\mathbf{h}'_c, \mathbf{h}''_c$ as proposed in **Friston (1998)**. The generative model, illustrated in Fig. 1(a), reads:

$$\forall j, \quad \mathbf{y}_j = \sum_{m=1}^M \mathbf{X}^m (\beta_j^m \mathbf{h}_c + \beta'_j{}^m \mathbf{h}'_c + \beta''_j{}^m \mathbf{h}''_c) + \mathbf{P}\ell_j + \mathbf{b}_j, \quad (2)$$

where $\beta_j^m, \beta'_j{}^m, \beta''_j{}^m$ are the unknown effects associated with the m^{th} stimulus-induced regressors constructed with the fixed known vectors $\mathbf{h}_c, \mathbf{h}'_c, \mathbf{h}''_c$ respectively. To obtain the classical GLM with only the canonical HRF, β'_j and β''_j can be set to zero for all positions. **It is worth noting that this formulation of**

⁴ Note that the RFIR approach with supervised regularization is much faster with an analysis duration of 20 min. since the maximum a posteriori estimator admits a closed form expression.

Table 1. Comparative overview for all detection/estimation analysis procedures available in `pyhrf` in terms of model structure and analysis duration. “2nd order deriv.” stands for a penalization on the energy of the HRF which penalizes abrupt shape changes. The number of nuisance parameters was considered the same for all models, so that only the modeling of the stimulus-induced component is relevant to assess model parsimony. The ratio “unknowns / data” is given for a typical fMRI data analysis with $J = 4 \times 10^4$, $R = 3$, $D = 40$, $M = 10$, $\Gamma = 400$ and $N = 128$ (total number of data points: $N \times J$). The analysis duration is for a whole brain data treatment on an Intel Core i5 (M480 2.67Ghz).

	BS GLM smoothing	FIR GLM smoothing	RFIR smoothing	JDE adaptive
Spatial regularization	smoothing	smoothing	smoothing	adaptive
Temporal regularization	none	none	2 nd order deriv.	2 nd order deriv.
HRF shape constraint	function basis	free	smooth	smooth
Number of unknowns for the stimulus-induced component	$J \times R \times M$ $1 \leq R \leq 3$	$J \times D \times M$ $D \approx 10$	$J \times M \times (D+1)$ $10 \leq D \leq 50$	$2 \times J \times M + \Gamma \times (D+4M+1)$ $10 \leq D \leq 50$, $\Gamma \approx 400$
Typical ratio of unknowns / data	0.23	0.78	3.4	0.16
Analysis duration	3 min.	5 min.	30 h.	8 h.

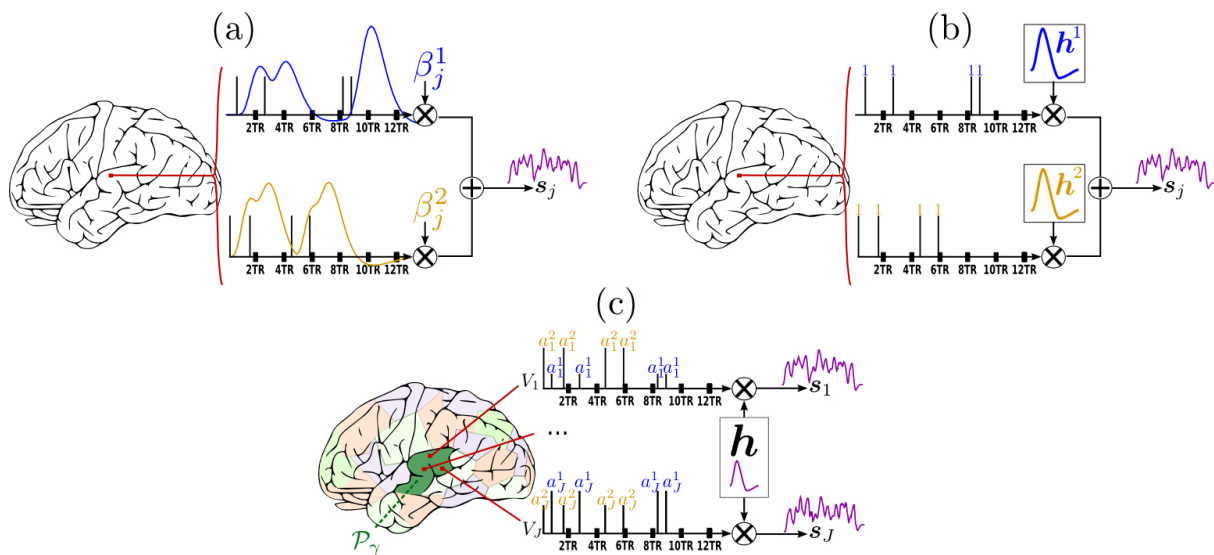


Figure 1. Forward models generating the stimulus-induced components for the methods available in `pyhrf`. In all cases, the scheme involves two experimental conditions colored in blue and yellow with four stimulation events as depicted by vertical bars over the TR-sampled grid. **(a):** General Linear Model (GLM). For a given condition in a given voxel, the stimulus event sequence is convolved with the fixed canonical HRF resulting in a fixed stimulus-induced regressor. This regressor is then multiplied by an unknown effect β_j^m . All the condition-specific regressors are then summed to form the final stimulus-induced signal s_j . **(b):** Finite Impulse Response (FIR) Model. In a given voxel, the stimulus event-sequence is convolved with an unknown FIR vector h^m for each condition to yield a condition-specific component. All components are then summed to form the final stimulus-induced signal s_j . **(c):** Joint Detection-Estimation (JDE). For a given voxel in a given parcel \mathcal{P}_γ , the stimulus sequence gathering all experimental conditions is multiplied by the response levels $\{a_j^m\}$. Then, this spike signal is convolved with an unknown spatially-invariant HRF h to form the stimulus-induced signal s_j .

the forward model is equivalent to the classical one where all regressors are gathered in the design matrix (noted \bar{X}) and all corresponding effects gathered in a single vector $\bar{\beta}$. Eq. (2) reads:

$$\forall j, \quad \mathbf{y}_j = \bar{X} \bar{\beta}_j + \mathbf{b}_j, \tag{3}$$

$$\text{with: } \bar{X} = [\mathbf{X}^1 \mathbf{h}_c \mid \dots \mid \mathbf{X}^m \mathbf{h}_c \mid \mathbf{X}^1 \mathbf{h}'_c \mid \dots \mid \mathbf{X}^m \mathbf{h}'_c \mid \mathbf{X}^1 \mathbf{h}''_c \mid \dots \mid \mathbf{X}^m \mathbf{h}''_c \mid \mathbf{P}]^T,$$

$$\bar{\beta}_j = [\beta_j^1 \mid \dots \mid \beta_j^m \mid \beta_j^{1'} \mid \dots \mid \beta_j^{m'} \mid \beta_j^{1''} \mid \dots \mid \beta_j^{m''} \mid \ell_j]^T.$$

175 The hemodynamics fluctuations caught by such a model are limited to ~ 1 second around the peak of the
 176 canonical HRF which is at 5 sec, see **Calhoun et al. (2004)**. This model is massively univariate since every
 177 position j is analyzed independently, i.e., no correlation between neighboring signals is considered. It
 178 works well on spatially smoothed data to counter-balance the low signal-to-noise ratio, at the expense of
 179 blurred activation clusters. In the `nipy` implementation of the GLM, the fitting process can be performed
 180 using ordinary least square in the case of white Gaussian noise or using Kalman filtering in the case of an
 181 $AR(1)$ Gaussian noise process.

2.2.2 FIR GLM and Regularized FIR

The generative BOLD signal modeling in the FIR context encodes all HRF coefficients as unknown variables:

$$\forall j, \quad \mathbf{y}_j = \sum_{m=1}^M \mathbf{X}^m \mathbf{h}_j^m + \mathbf{P} \ell_j + \mathbf{b}_j \quad (4)$$

182 Here, vector $\mathbf{h}_j^m = (h_{j,d\Delta t}^m)_{d=0,\dots,D}^t$ represents the unknown HRF time course in voxel j which is
 183 associated with the m^{th} experimental condition and sampled every Δt . In its un-regularized version,
 184 the FIR model can be expressed in the GLM framework and hence its implementation in `pyhrf` relies on
 185 `nipy`.

186 In the case of the Regularized FIR (**Ciuciu et al. (2003)**), the problem is placed in the Bayesian
 187 formalism in order to inject regularity on the recovered HRF coefficients \mathbf{h}_j . More specifically, $\mathbf{h}_j^m \sim$
 188 $\mathcal{N}(\mathbf{0}, v_{\mathbf{h}_j^m} \mathbf{R})$ with $\mathbf{R} = (\mathbf{D}_2^t \mathbf{D}_2)^{-1}$ where \mathbf{D}_2 is the second-order finite difference matrix enforcing local
 189 smoothness by penalizing abrupt changes quadratically and $v_{\mathbf{h}_j^m}$ is the unknown HRF prior variance which
 190 is jointly estimated. Computational and inference details are given in **Ciuciu et al. (2003)**.

2.2.3 Joint Detection-Estimation

192 The functional mask of a given subject's brain is a priori divided in Γ functionally homogeneous *parcels*
 193 using methods described in subsection 2.3.2. In each parcel \mathcal{P}_γ , the shape of the HRF \mathbf{h}_γ is assumed
 194 constant and the parcel-specific generative model reads:

$$\forall j \in \mathcal{P}_\gamma, \quad \mathbf{y}_j = \sum_{m=1}^M a_j^m \mathbf{X}^m \mathbf{h}_\gamma + \mathbf{P} \ell_j + \mathbf{b}_j. \quad (5)$$

195 where \mathbf{y}_j , \mathbf{X}^m , \mathbf{P} , ℓ_j and \mathbf{b}_j match the variables introduced in subsection 2.2.1. As shown in Fig. 1(c)
 196 which illustrates this forward model, the a_j^m variables encode fluctuations that occur *before* the application
 197 of the hemodynamic filter. Therefore, they are assimilated to neural effects and referred to as “Neural
 198 Response Levels” (NRL). However, this term, which is historical, might be misleading as it is difficult
 199 to disentangle the contribution of the neural and the vascular components from single BOLD fMRI data.
 200 [These variables can be more simply identified to the voxel- and condition-specific response amplitudes.](#)

201 In contrast to Eq. (2) for the GLM forward model, the fixed HRF components \mathbf{h}_c and \mathbf{h}'_c are replaced
 202 by an *unknown* parcel-based HRF \mathbf{h}_γ . Similarly, each unknown NRL a_j^m embodies a single magnitude
 203 parameter per regressor whereas the GLM formulation implies that the magnitude is distributed between
 204 weights β_j^m , $\beta_j^{m'}$ and $\beta_j^{m''}$. To summarize, the HRF shape and the BOLD response magnitude are coupled
 205 in the GLM formulation whereas they are decoupled in the JDE formulation.

206 In the Bayesian framework, priors are formulated to (i) enforce temporal smoothness on the HRF shape
 207 [to perform estimation](#) in the same manner as for RFIR and (ii) account for spatial correlations between

208 NRLs through spatial mixture models [to perform detection](#), as described in [Vincent et al. \(2010\)](#). The
209 regularization factor that controls the amount of spatial regularization is jointly estimated and optimized
210 wrt parcel topology so as to perform an adaptive spatial smoothing. If the experimenter is not interested
211 in the estimation of the HRF, then the HRF can be fixed typically to its canonical version in the JDE
212 framework which hence amounts to a *spatially adaptive GLM*. [The latter approach enables parcelwise](#)
213 [multivariate detection of activations with adaptive regularization across parcels](#). As shown at the group-
214 [level in Badillo et al. \(2013b\)](#), this strategy retrieves more peaked and less extended activation clusters
215 [compared to classical SPM-like analysis](#).

216 The inference is performed by a stochastic sampling scheme where posterior mean estimates are
217 computed from Markov Chain Monte Carlo samples. The implementation of the main sampling loop
218 is coded in pure python and some intensive samplers such as the one for the HRF of the NRLs are
219 coded in C. Still, the overall JDE procedure is computationally demanding. However, since there are as
220 many *independent* models as parcels, the analysis can be split up into parcel-wise *parallel* analyses (see
221 section 3.3). The efficiency of the inference scheme has [also](#) been improved by resorting to a variational
222 formulation of the JDE [Chaari et al. \(2013\)](#) which is also available in `pyhrf`.

2.3 PARCELLATION

2.3.1 Spatial parcellation

224 *Random Voronoi diagrams* A Voronoi diagram consists of a spatial partitioning that builds parcels around
225 predefined control points or seeds. The parcel boundaries are placed so that each point of a given parcel
226 is closer to the associated parcel seed than any other seed in terms of the Euclidean distance, as illustrated
227 in Fig. 2(left). To build a parcellation from such partitioning, i.e., to assign each cerebral position to a
228 parcel identifier, we do not explicitly require the parcel boundaries. Accordingly, there is no need to rely
229 on classical algorithms that precisely compute these boundaries. Instead, a given position is assigned to
230 the closest seed by resorting to a kd-tree⁵.

231 Random Voronoi parcellations are convenient ways to generate samples in the space of sensible
232 parcellations as they produce convex and compact parcels which are physiologically plausible. They have
233 been used in [Vincent et al. \(2008\)](#) to study the sensitivity of the parcel-based JDE method.

234 *Balanced partitioning* The goal of balanced partitioning is to build parcels of equal sizes. In the case of
235 a non-regular topology such as the brain, there is no morphological tool to deterministically solve such
236 partitioning problem which is known to be NP-complete as mentioned in [Andreev and Racke \(2004\)](#).
237 Hence, the algorithm implemented in `pyhrf` employs a heuristic and relies on a multi-agent system
238 that mimics the inflation of balloons in a fixed volume ([Elor and Bruckstein \(2009\)](#)), as illustrated in
239 Fig. 2(right).

240 Balanced partitioning is useful to test the effect of parcel size. In `pyhrf`, balanced partitioning is
241 implemented in pure python with a position-wise main loop and is hence rather slow: ~ 1 minute to
242 split 6000 voxels into 20 parcels. However, this performance is sufficient since we only employ balanced
243 partitioning in the case of small scale testing data sets or when parcels obtained on real data are too big.

2.3.2 Functional parcellation

245 The main goal of functional parcellation is to provide homogeneous parcels with respect to
246 hemodynamics. It is mainly motivated by the JDE procedure which assumes that the HRF shape is
247 constant within one parcel. To provide such parcellation, results obtained from a GLM analysis, [or any](#)
248 [given task-specific functional maps](#) are clustered using different available algorithms: K-means, Ward or

⁵ implemented in `scipy.spatial.KDTree`

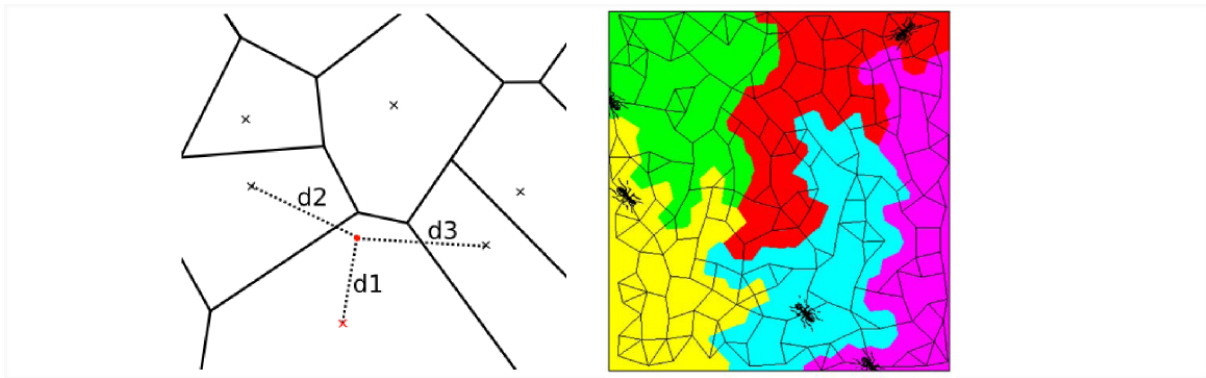


Figure 2. Illustration of spatial parcellation methods in `pyhrf`. **Left:** Voronoi diagram where seeds are represented as crosses. The red point is assigned to the red seed and verifies that its distance to any other seed is larger ($d1 < d2$, $d1 < d3$). **Right:** balanced partitioning performed by patrolling a(ge)nts, image extracted from Elor and Bruckstein (2009).

249 spatially-constrained Ward as provided by `scikit-learn`⁶. To objectively choose an adequate number
 250 of parcels, theoretical information criteria have been investigated in Thyreau et al. (2006): converging
 251 evidence for $\Gamma \approx 400$ at a spatial resolution of $3 \times 3 \times 3 \text{ mm}^3$ has been shown for a whole brain
 252 analysis leading to typical parcel sizes around a few hundreds voxels ($\approx 2.7 \text{ cm}^3$). As the parcel size is not
 253 fixed, some big parcels may arise from the parcellation process and may slow down the overall parallel
 254 processing. To overcome this, the maximum parcel size was controlled by splitting too big parcels (larger
 255 than 1000 voxels) according to the balanced partitioning presented in section 2.3.1, which also guarantees
 256 the spatial connexity and thus properly satisfies the JDE assumptions on the HRF.

257 Such “hard clustering” approach yields sharp parcel boundaries that prevent from capturing smooth
 258 transitions between HRF territories. To avoid wrong boundaries, one can resort to over-segmented
 259 parcellations (high number of parcels).

3 PYHRF

260 The installation of `pyhrf` relies on the `setuptools` python package and requires the following
 261 dependencies: `numpy`⁷ and `scipy`⁸ for core algorithms, `nibabel` for nifti or gifti input/outputs, `nipy`
 262 for the GLM implementation and parcellation tools, `matplotlib` for plots and `PyQT4` for GUIs.
 263 Optional dependencies comprise `joblib`, `scikit-learn` and `soma-workflow`. `pyhrf` is mainly
 264 intended for linux-based distributions as it has especially been developed under Ubuntu. Installation
 265 notes and documentation can be found online at <http://www.pyhrf.org>. Withing the package,
 266 the following data files⁹ are shipped:

- 267 • 2 volumic fMRI data sets (paradigm as CSV files, anatomical and BOLD data files). One serves
 268 quick testing while the other is intended for validation/demonstration purpose, which is used to
 269 generate results in section 4.3,
- 270 • 1 surfacic fMRI data set mainly intended for testing,
- 271 • several simulation resources in the form of `png` images to provide 2D maps of various activation
 272 labels and HRF territories.

⁶ `sklearn.cluster.ward`

⁷ www.numpy.org

⁸ www.scipy.org

⁹ There is no special licence on the shipped data sets.

273 The rest of this section is organized as follows. First, the overall workflow of how to use `pyhrf` is
 274 presented, which mainly resorts to command lines and some dedicated GUI tools. Second, to go further
 275 into the package architecture and also to address some features available when scripting, the design of
 276 `pyhrf` is introduced. Third, distributed computation is explained in terms of resource handling. Finally,
 277 the `pyhrf` viewer is presented with a focus on ergonomics.

3.1 WORKFLOW

278 The typical usage of `pyhrf` relies on shell commands which work on XML files. This XML format
 279 was chosen for its hierarchical organization which suits well the nested nature of the algorithm
 280 parametrizations. A dedicated XML editor is provided with a `PyQt4` graphical interface for a quicker
 281 edition and also a better review of the treatment parameters. When such an XML setup file is generated,
 282 it defines a default analysis which involves a small volumic real data set shipped with the package. This
 283 allows for a quick testing of the algorithms and is also used for demonstration purpose. Here is a typical
 284 example of shell commands sequence used to perform a JDE analysis:

```
$ pyhrf_jde_buildcfg -o jde.xml      # generate a default XML file
$ pyhrf_xmledit jde.xml            # set up custom experiment
$ pyhrf_jde_estim -c jde.xml       # run the analysis
$ pyhrf_view *nii                 # view all output nifti files
```

285 The “`buildcfg`” command offers various options to define setup items from the command line without
 286 having to edit the XML file. For example, the paradigm can be loaded from a CSV or a SPM.mat file.
 287 As for the JDE procedure specifically, the option `--vem` enables the variational EM approach developed
 288 in **Chari et al.** (2013).

3.2 DESIGN

289 An overview of the static design of the main package components of the package is shown in Fig. 3. The
 290 class `FmriData` is the within-subject fMRI data representation, for any spatial support: on the cortical
 291 surface, in the volume, or from a simulation. [This data representation](#) comprises spatially flat data (fMRI
 292 time series and parcellation) and a connectivity matrix which holds the data topology. At the centre of the
 293 analysis component is the `Analyzer` class that handles parcelwise data splitting which is done according
 294 to the input data parcellation by default, and also takes care of merging parcel-specific outputs at the end
 295 of the analysis. This `Analyzer` class is then specialized into various method-specific analyzers: GLM,
 296 RFIR and JDE. Note that the analyzer component is decoupled from the data component, as classically
 297 done in scientific programming because they do not have the same life-cycles (e.g., the same model can be
 298 applied to various data objects). The `FmriTreatment` packs the data and analysis definitions together
 299 and handles distributed computation across parcels.

300 In the following sub-sections, two specific components are further explained: XML parametrization
 301 through the `XmlInitable` class, and the handling of arrays with axis semantics through the `xndarray`
 302 class.

303 **3.2.1 XML parametrization** The XML format was chosen for its hierarchical organization which suits
 304 the nested nature of the algorithm parametrizations. Indeed, for a JDE analysis, here is an example of
 305 such different levels: `treatment` → `analyzer` → `sampler` → `hrf_sampler`. At a given level,
 306 different classes may be used as there exist, for example, different `sampler` types depending on the type
 307 of prior expressed in the JDE model, so that we require a seamless parametrization process that avoids
 308 rewriting code for the building of parameter files each time a new model is tested. To do so, any object
 309 whose initialization has to be exposed in the XML configuration file inherits the `XmlInitable` class.
 310 This system is not a serialization process as the whole python object is not dumped in the XML. Only the

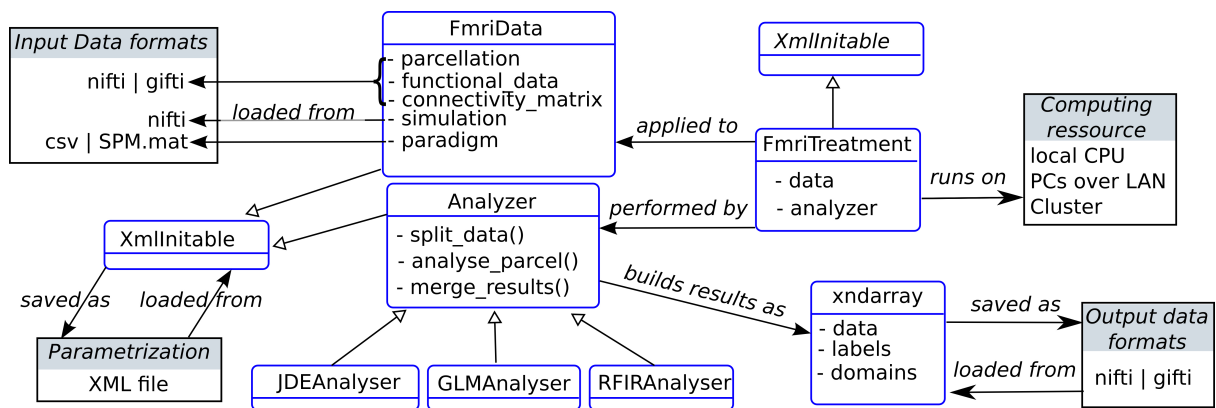


Figure 3. Static organization of the main components in the pyhrf package (not exhaustive). Classes are represented as rounded blue rectangles and external resources (file, computing units) as black rectangles. Note that the XmlInitable class is duplicated for layout convenience. As in UML class diagrams, arrows have the following meaning: → stands for an association, → stands for a generalization.

```

from pyhrf.xmlio import XmlInitable, to_xml
import numpy as np

class FmriTreatment(XmlInitable):
    def __init__(self, input_data=None,
                 analysis_parameters=None):
        XmlInitable.__init__(self)

data = { 'bold_file' : './my_bold.nii',
        'paradigm' : np.array([0,2.3,6.]) }

analysis = { 'model' : 'JDE_MCMC',
            'mcmc_sampling' : {
                'HRF' : { 'duration' : 25,
                        'type' : 'canonical' }}}

treatment_xml = to_xml(FmriTreatment(data, analysis))
f = open('./test.xml','w')
f.write(treatment_xml)
f.close()
    
```

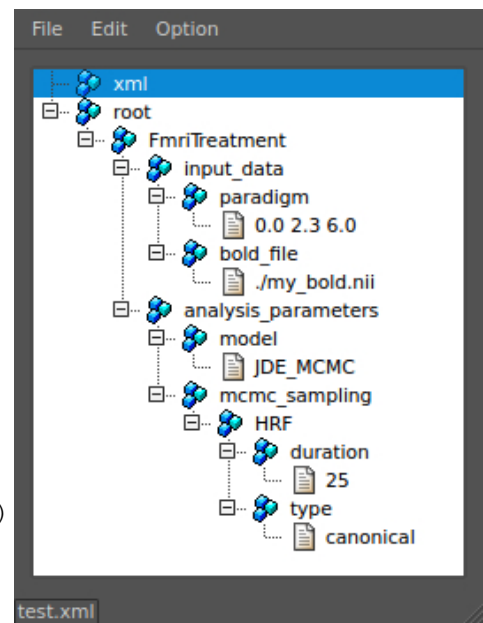


Figure 4. Handling of XML parametrization. The left part shows a code snippet that defines a dummy yet typical fMRI treatment structure with nested components. The init process of the resulting top-level object is then saved in an XML file. The right part is a snapshot of the pyhrf_xmledit main window where the XML file generated by the code snippet is browsed.

311 parameters provided to the `__init__` function are stored. In terms of object life cycle, this process handles
 312 object creation but is not able to track any subsequent modification. Fig. 4 shows a python code sample
 313 that illustrates how the XML file is generated from this nested configuration situation. The resulting XML
 314 file as viewed by the command `pyhrf_xmledit` is also displayed.

315 **3.2.2 The xndarray class: data array with axis semantics** The development of semantics-driven
 316 operations on data arrays were motivated by the parcel-driven nature of the analysis workflow which
 317 implied that parcel-specific results have to be merged in a transparent fashion, whatever their shape.
 318 Indeed, as pyhrf is the repository of all the methodological tools developed within the JDE framework,
 319 the number and the form of outputs is highly changing during the development and testing process.

320 This involves producing convergence tracking, intermediate quantities in addition to the final results
 321 of interest. To avoid writing specific saving procedure for such versatile and numerous outputs, the
 322 information about the interpretation of the data axes has to be explicit. The class `xndarray` handles
 323 any required reorientation prior to saving data arrays into nifti or gifti files. In the volumic data case, the
 324 reorientation follows the `nibabel` convention that is sagittal, coronal, axial and time. To store the extra
 325 axis information along with the data, a dedicated nifti-extension is also written in the volumic data case
 326 or add a “`pyhrf_xndarray_data`” field in the gifti meta data dictionary in the surfacic data case.

327 Moreover, outputs are primarily generated at the parcel-level so that they are in a flat shape, i.e., the
 328 position axis represent indexes of positions in the spatial domain. To form the final whole brain outputs,
 329 the parcel-specific outputs have to be merged together and the position axis, if present, has to be mapped
 330 into the final spatial domain. Table 2 shows two examples of parcel-specific outputs that are merged to
 331 form whole brain data either by spatial mapping or by parcel stacking. To handle these two merging
 332 operations, `stack` and `merge` functions are provided. The reverse process is also available via the
 333 method `explode` which allows an array to be split according to a mask composed of integers, i.e. a
 334 parcellation. It returns the dictionary of ‘flat’ parcel-specific data arrays associated with each integer label
 335 present in the mask.

336 In terms of data life cycle, `xndarray` objects are used to prepare data before analysis and to
 337 pack results after analysis. During the analysis process, it is more convenient to work with `numpy`
 338 arrays directly. The following code snippet illustrates the usage of `xndarray` objects: functional and
 339 parcellation data are loaded, within-parcel means are computed and the results is saved to nifti:

```

from pyhrf.ndarray import xndarray, merge
# Data loading
func_data = xndarray.load('./bold.nii')
parcellation = xndarray.load('./parcellation.nii')
# Split functional data into parcel-specific data
parcel_fdata = func_data.explode(parcellation)
# Fill parcel-specific data with spatial means
parcel_means = dict( (parcel_id, d.copy().fill(d.mean('position')) )
                    for parcel_id, d in parcel_fdata.items() )
# Merge parcel-specific means (map 'position' axis onto spatial axes)
parcel_means = merge(parcel_means, parcellation, axis='position')
# Save output
parcel_means.save('./bold_parcel_means.nii')
    
```

Table 2. Examples of merging operations performed on multiple parcel-specific data arrays, for some JDE outputs: parcel-specific HRFs and condition- and voxel-specific activation labels. If the `xndarray` object contains the “position” axis, as for the “labels” object, then all parcel-specific results are merged into the same target volume and we depict the spatial mapping operation as “→” to map the “position” axis in to the spatial axes “axial”, “coronal” and “sagittal”. For other axes aside from “position”, no merging operation is performed (“=” symbol). If the `xndarray` object does not contain the “position” axis, as for the HRF object, then all parcel-specific results are stacked and a new “parcel” axis is created (“U” symbol).

	Parcel-specific flat data		Merging operation	Whole brain data	
	axis label	axis domain		axis label	axis domain
HRF	time	[0, ..., hrf_duration]	=	same	
			U	parcel	[0, ..., parcel_max]
labels	class	['activ', 'non_activ']	=	same	
	condition	['audio', 'video']	=	same	
	position	[0, ..., pos_max]	→	axial	[0, ..., axial_max]
				coronal	[0, ..., coronal_max]
				sagittal	[0, ..., sagittal_max]

3.3 DISTRIBUTED COMPUTING

340 PyHRF provides parallel processing features by exploiting local resources (multiple processors on a single
341 workstation) as well as remote parallel processing units such as a local grid network or a cluster. A whole
342 brain JDE analysis then boils down from 10 hours to 15 minutes in parallel (on a 100-cores cluster). More
343 precisely the available computing resources are handled as follows:

- 344 • **local multiple-cores CPUs:** through the use of `joblib` parallel features. The latter works by
345 spawning python sub-processes that are then run on the different processing units by the operating
346 system. The number of used CPUs can be setup by the user.
- 347 • **machines over a local area network:** through in-house code that relies on `paramiko` and
348 hence uses `ssh` connections to distribute jobs on the LAN. A basic scheduler is implemented in
349 `pyhrf.grid` that can also report faulty remote runs.
- 350 • **multiple-cores cluster:** through `soma-workflow`¹⁰ developed by **Laguitton et al.** (2011), which
351 relies on `paramiko`¹¹ on the client side and on `DRMAA`¹² on the server side.

352 The distribution problem addressed here is a so-called embarrassingly parallel problem where the same
353 treatment has to be repeated on several parcel-specific pieces of data. There is no shared memory
354 management between distributed processes here.

355 To optimize the distribution process, the order in which the parcel-specific treatments are pushed in the
356 process queue is done by pushing the biggest parcels first. In the same optimization purpose, a safeguard is
357 imposed on the maximum parcel size (more than 7 cm³ in the volume or 11 cm² on the surface). If a parcel
358 exceeds this limit, it is divided up according to the balanced partitioning presented in sub-section 2.3.1.

3.4 VIEWER

359 `pyhrf_view` is a dedicated viewer built on `PyQt4` which embeds a `matplotlib` view. The purpose
360 of `pyhrf_view` is to provide convenient browsing into volumic data¹³. However, it does not provide
361 advanced overlaying features such as the display of functional over anatomical data. Instead, to plot the
362 final “publication-ready” maps after having selected the results of interest with `pyhrf_view`, one can resort
363 to the command `pyhrf_plot_slice` to directly generate a slice image of functional rendering along with
364 anatomical overlay. One can also use a third party viewer such as `Anatomist`¹⁴, `FSL_view`¹⁵ or `xjview`¹⁶.

365 `pyhrf_view` offers n-dimensional browsing while most viewers in neuro-imaging software handle up
366 to 4D volumes. In fact, there is a limit to the number of dimensions inherent to the `nifti` format which
367 permits 7 axes at maximum. The viewer is composed of two main components (see 5:

- 368 • a main window handling object and slice selection,
- 369 • plot windows which display the selected slice as curve or image.

370 The slice selection tools provides sliders to browse through axes domain values and display related
371 information: axis name, current selected domain values and projection states. There can be up to two
372 projected axes (2D), i.e., axes which will mapped to the actual plot axes. When multiple objects are loaded,

¹⁰ <http://brainvisa.info/soma-workflow/>

¹¹ <http://www.lag.net/paramiko/>

¹² <http://www.drmaa.org/>

¹³ Surface rendering is not available. `Anatomist` is recommended for such usage

¹⁴ <http://brainvisa.info>

¹⁵ <http://fsl.fmrib.ox.ac.uk/fsl/fslview/>

¹⁶ <http://www.alivelearn.net/xjview8/>

373 slicers are synchronized to plotting views so that click events yield slider updates. This behavior can be
 374 modified in two ways. First, the reception combo box toggles whether the slider receives changes from
 375 other sliders. This is useful when one wants to prevent a given view from being updated by synchronization
 376 events (with reception off), e.g., when a reference slice should be compared to other slices. Second, the
 377 emission combo box toggles the spreading of slider changes to all other slicers. This is typically used to
 378 control a given axis across all displayed objects with a single slider (with emission on).

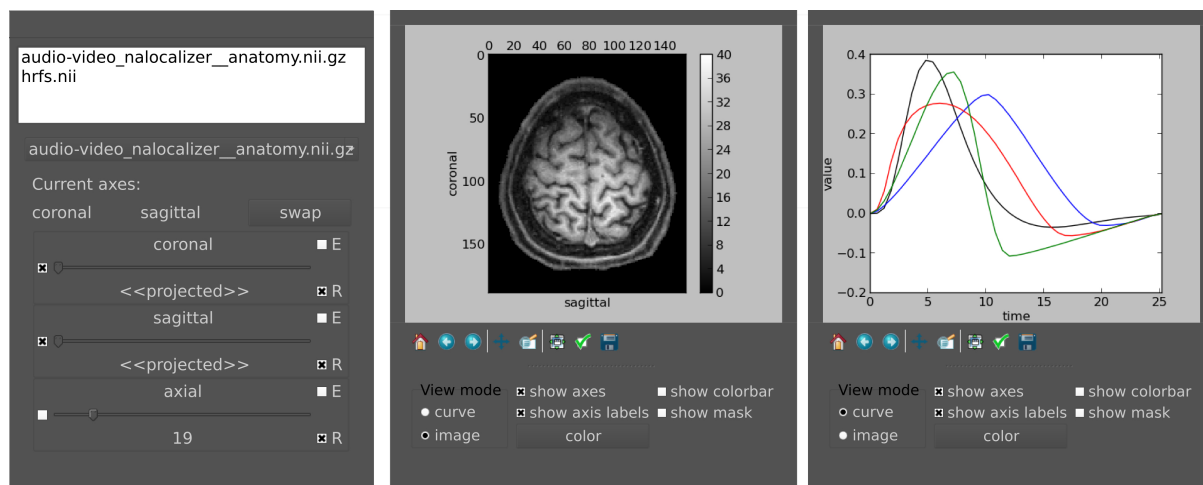


Figure 5. Main widget components of `pyhrf_view` to browse and view n-dimensional data. **Left:** the list widget on top displays the currently loaded objects. The slicer panel at the bottom allows: projection of axes (combo boxes on the left), domain value slicing (sliders in the middle) and definition of view synchronization (combo boxes on the right). For a given axis slicer, the two combo boxes defining synchronization are: (E) toggle emission of slice change to other slicers, (R) toggle reception from other slicers or from click events on plots. **Middle:** plot window for the current selected slice. The top part displays the actual plot as produced by `matplotlib.pyplot`. The bottom part offers changing the view mode (either curve, image, or histogram), and toggling display of axes, colorbar and mask. The color button pops up a gradient map selector if in image mode or a color picker if in curve mode. **Right:** other plot window to illustrate curve display.

4 RESULTS

4.1 EXPERIMENTAL PARADIGM

379 In all presented results, whether they focus on artificial or real data sets, we resorted to the same
 380 experimental paradigm. The latter is a multi-functional cognitive localizer paradigm designed in **Pinel**
 381 **et al.** (2007). This paradigm enables to map cognitive brain functions such as reading, language
 382 comprehension and mental calculations as well as primary sensory-motor functions. It consists of a *fast*
 383 *event-related* design (sixty stimuli, $ISI = 3.75$ sec.) comprising the following experimental conditions:
 384 auditory and visual sentences, auditory and visual calculations, left/right auditory and visual clicks,
 385 horizontal and vertical checkerboards.

4.2 ARTIFICIAL DATA GENERATOR

386 Simulations in `pyhrf` mainly consists of building a script that defines a pipeline of versatile simulation
 387 bricks presented in Table 3. Writing a simulation script as a sequence of functions makes things difficult
 388 to read and to reuse. Instead, all simulation bricks are gathered inside a python dictionary that maps a
 389 simulation label to its corresponding value. This value can be directly defined as a python object or as a
 390 function which can depend on other simulation items and which is called when the simulation pipeline is

391 evaluated. The pipeline structure arises from the link between simulation labels and function arguments.
 392 An example of such simulation script is given below:

```
import numpy as np
from pyhrf.ndarray import xndarray
from pyhrf.tools import Pipeline

# Functions used to generate items in the simulation Pipeline
def generate_rls(spatial_shape, mean_rls, var_rls):
    rls = np.random.randn(*spatial_shape) * var_rls**.5 + mean_rls
    return xndarray(rls, ['axial', 'sagittal', 'coronal'])

def generate_noise(stim_induced_signal, noise_var):
    noise = np.random.randn(*stim_induced_signal.data.shape) * noise_var**.5
    return xndarray(xndarray_like(stim_induced_signal, data=noise))

def create_stim_induced_signal(rastered_paradigm, hrf, response_levels):
    signal = np.convolve(rastered_paradigm, hrf)[np.newaxis,:] * \
        response_levels.data[:, :, :, np.newaxis]
    return xndarray(signal, response_levels.axes_names + ['time'])

def create_bold(stim_induced_signal, noise):
    return stim_induced_signal + noise

# Definition of the simulation pipeline
simulation_steps = {
    'spatial_shape' : (10,11,12), 'mean_rls' : 3., 'var_rls' : 0.5,
    'response_levels' : generate_rls,
    'rastered_paradigm' : np.array([0,0,1,0,0,0,1,0,0,0,1]),
    'hrf' : np.array([0, .5,1,0.5,0.,0]),
    'noise_var' : 1.,
    'noise' : generate_noise,
    'stim_induced_signal' : create_stim_induced_signal,
    'bold' : create_bold,
}

simulation = Pipeline(simulation_steps)

# Computation of all quantities in the pipeline and data saving
simulation.resolve()
simulation_items = simulation.get_values()
simulation_items['response_levels'].save('./response_levels.nii')
simulation_items['stim_induced_signal'].save('./stim_induced_signal.nii')
simulation_items['bold'].save('./bold.nii')
```

393 The artificial data experiment presented here comprises the generation of BOLD time series within the
 394 volume and then projected onto the cortical surface. To do so, shipped data defines a volume of 4 HRF
 395 territories, as well as the grey/white matter segmentation obtained from real data in the occipital region.
 396 Within the grey matter mask, activation labels are generated and conditionally to them, response levels
 397 are simulated according to a bi-Gaussian mixture. For the sake of simplicity, a version of the localizer
 398 paradigm presented in the previous section is merged over the auditory and visual modalities so as to
 399 obtain only two conditions. In all HRF territories this paradigm is then convolved with HRF generated by
 400 Bezier curves that enable the control of the time-to-peak and time-to-undershoot. Finally, nuisance signals
 401 are added (Gaussian noise and polynomial drift) to obtain the volume of artificial BOLD data. To generate
 402 surfacic data, data are projected on a cortical fold that is also shipped in the package and we resorted to an
 403 external projection tool, developed in **Operto et al.** (2006) but others are available such as `Freesurfer`.

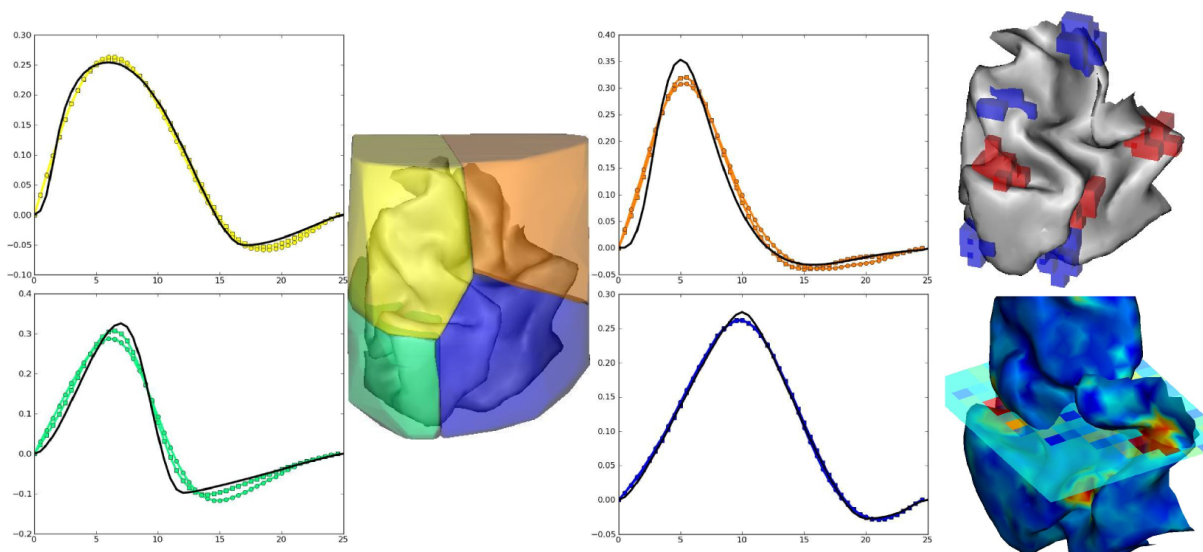


Figure 6. Results on volumic and surfacic artificial data. **Left part:** HRF estimates obtained by JDE on the 4 artificial parcels. Ground truth HRFs are depicted in black line while colored HRF are HRF estimates that match the color of the parcels. **Right part, top:** labels simulated in the cortical fold for two conditions (in blue and red). **Right part, bottom:** response levels estimates obtained by JDE on the cortical surface and in a selected slice of the volume. 3D renderings were produced with `anatomist`.

404 Fig. 6 presents the results obtained on artificial data using the JDE procedure. HRF estimates recover their
 405 respective ground truth profiles with a slightly more deformed curve obtained on the cortical surface for
 406 the bottom right (green) HRF territory, compared with the volumic data case. Detection results (response
 407 levels maps in Fig. 6) also shows the correct recovery of the simulated ground-truth, in the volume and on
 408 the cortical surface.

4.3 WITHIN-SUBJECT METHOD COMPARISON

409 The analyzed real data set, which is shipped with `pyhrf`, was a subset of an fMRI acquisition performed
 410 on a single healthy subject with a 3-Tesla Tim Trio Siemens scanner using an EPI sequence. The following
 411 settings were used for this acquisition: the fMRI session consisted of $N = 128$ scans, each of them being
 412 acquired using $TR = 2400$ ms, $TE = 30$ ms, slice thickness: 3 mm, $FOV = 192 \text{ mm}^2$ and spatial in-plane
 413 resolution of $2 \times 2 \text{ mm}^2$. In order to reduce disk usage and to focus only on areas of the brain which are
 414 expected to elicit activity in response to the paradigm, functional data was restricted to selected regions of
 415 interest that comprise occipital, temporal, parietal and motor regions. To improve interpretation and data

Table 3. Different types of simulation bricks available in `pyhrf`. The “localizer” paradigm is described in [Pinel et al. \(2007\)](#). Hand-drawn maps for activation labels are in the form of `png` images. Gaussian smooth generation of HRFs stands for the regularized prior used in the JDE model.

Simulation item	available generation process
Experimental paradigm	localizer, random event-related
Activation labels	hand-drawn 2D maps, 3D Potts realizations
Response levels	bi / tri mixture of Gaussian or Gamma components
Hemodynamic response function	canonical, Bezier curve, Gaussian smooth
Low frequency drift	polynomial, cosine
Noise	white, auto-regressive of order p

416 plot rendering, an anatomical image is also shipped, with an in-plane resolution of $1 \times 1 \text{ mm}^2$ and slice
417 thickness of 1.1 mm.

418 This fMRI data set was analyzed using GLM with a canonical HRF, FIR, RFIR and JDE¹⁷. For JDE, the
419 functional parcellation was built according to the method described in section 2.3.2. Fig. 7(a-b) depicts
420 detection results for the auditory effect, obtained by GLM with canonical HRF (see Fig. 7(a)) and JDE
421 (see Fig. 7(b)). Both methods highlight the same activation localization, with a slightly stronger sensitivity
422 for JDE. Fig. 7(c) shows HRF estimation results as obtained by FIR, RFIR and JDE at the same local
423 maximum on the left temporal region. Note that the HRF estimate provided by the JDE procedure is
424 regional. The HRF profile delivered by FIR appears noisier than the JDE and RFIR counterparts. Also the
425 temporal resolution of FIR is limited to the TR of input data. In contrast, RFIR and JDE offer an enhanced
426 temporal resolution of 0.6 sec. In terms of timing, the FIR and JDE methods yield a peak at 5 seconds
427 which is compatible with the canonical HRF that has been fitted on temporal auditory regions (Boynnton
428 et al. (1996)). Accordingly, the HRF estimates obtained by RFIR seems over-smoothed. Overall, JDE
429 enables reliable activation maps and HRF profiles which can roughly be obtained by separate GLM and
430 FIR analyses. Fig. 7(d-e) shows results on effect maps for the computation effect, obtained by GLM with
431 canonical HRF (see Fig. 7(d)) and JDE (see Fig. 7(e)). JDE results have a higher sensitivity which can be
432 explained by an estimated HRF that differs from the canonical version (see Fig. 7(f)). More specifically
433 on the HRF estimation results shown in Fig. 7(f), we can draw the same comments as for the auditory
434 results. However, the FIR HRF profile is here more chaotic and its peak is less easy to identify as the
435 curve shows a plateau between 7 and 10 sec.

4.4 GROUP-LEVEL HEMODYNAMICS

436 Using `pyhrf`, the hemodynamic variability was also studied on a group of 15 healthy volunteers (average:
437 23.2 years, std: 2 years). The experimental paradigm is described in Section 4.1 and the fMRI acquisition
438 parameters are similar to those previously mentioned in subsection 4.3. The results presented hereafter
439 have been published in Badillo et al. (2013b). In this work, hemodynamic variability was investigated
440 in four regions of interest, located in the left parietal cortex (P), bilateral temporal (T) and occipital (O)
441 lobes and in the right motor cortex (M), as shown in Fig. 8. These regions were defined after conducting
442 a random-effect analysis to detect activation clusters showing a significant group-level effect. More
443 precisely, we defined four contrasts of interest targeting brain activity in sensory and cognitive regions:
444 a *Auditory vs. Visual* contrast for which we expect evoked activity in temporal regions in response, a
445 *Visual vs. Auditory* contrast that induces evoked activity in the occipital cortex, a *Left vs. Right click*
446 contrast for which we expect evoked activity in the right contralateral motor cortex, and a *Computation*
447 *vs. Sentence* contrast which is expected to highlight activity in the frontal and parietal lobes specific to
448 mental calculations. In terms of detection performance, at the group-level, JDE and GLM are comparable
449 in primary sensory regions (where the canonical HRF is appropriate). However, in the parietal region
450 involved in higher cognitive processes, the JDE approach yields more sensitive maps. In what follows, we
451 summarize group-level hemodynamics results obtained in the regions of interest extracted from activated
452 clusters.

453 The group-level HRF extraction in each ROI involves the following steps: For each subject, we
454 identified the parcel containing the mostly activated voxel across stimulus-dependent response levels.
455 Each individual parcel-based HRF time course is then scaled by the corresponding maximum response
456 level so as to account for the inter-subject variability of the effect size. Last, each group-level HRF
457 profile (see Fig. 8) is computed as the average over the 15 subjects in the corresponding ROI.

458 One of the main results concerns the spatial gradient of discrepancy to the canonical HRF shape between
459 regions. As shown in Fig. 8, the mean HRF time courses retrieved in occipital and temporal regions are the
460 closest to the canonical shape h_c . In the motor cortex, the HRF deviates a little more from the canonical

¹⁷ analysis scripts are available at <http://github.com/pyhrf/pyhrf/tree/master/script/frontiersBIM14/>

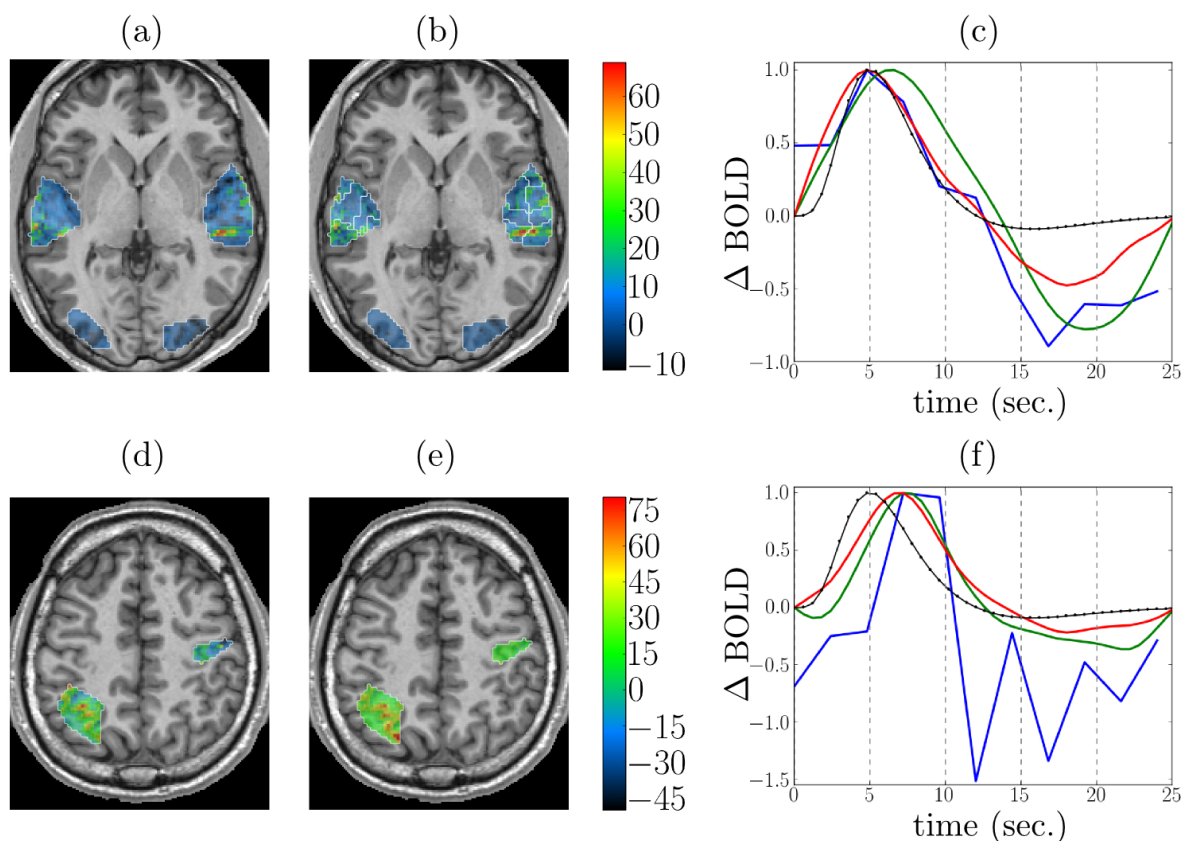


Figure 7. Detection and estimation results on the shipped real data set. Top and bottom rows: auditory and computation experimental conditions, respectively. Columns from left to right: response level maps, for (a,d) GLM with canonical HRF, (b,e) JDE, superimposed with the functional parcellation (white borders). Neurological convention: left is left. (c): Estimation results for GLM FIR (blue), RFIR (green) and JDE (red). The canonical HRF is shown in black.

461 filter, especially in terms of hemodynamic delay. Finally, the largest discrepancy to the canonical HRF
 462 was found in the parietal region.

5 PERSPECTIVES

5.1 METHODOLOGICAL PERSPECTIVES

463 The main methodological developments are currently taking place in the JDE framework. In fMRI
 464 activation protocols, the paradigm usually consists of several runs repeating similar sequences of stimuli.
 465 For an increased stability of HRF estimates that cope with the between-run variability of the response
 466 magnitude, a [hierarchical](#) multi-run extension with [heteroscedastic](#) noise has been developed in [Badillo
 467 et al. \(2013c\)](#). It is particularly useful for pediatric imaging where runs are short in time. In the same vein
 468 of improving within-subject analyses, an approach to encode the condition-specificity at the parcel level
 469 is being developed to enforce non-relevant conditions to yield null activation, as in [Bakhous et al. \(2013\)](#).

470 The variational EM version of JDE that has been published in [Chaari et al. \(2013\)](#) and that appeared
 471 to be 10 to 30 times faster than its MCMC alternative, has allowed us to address [Chaari et al. \(2012\)](#)
 472 the additional task of estimating the spatial aggregation support of HRF shapes (parcellation), which

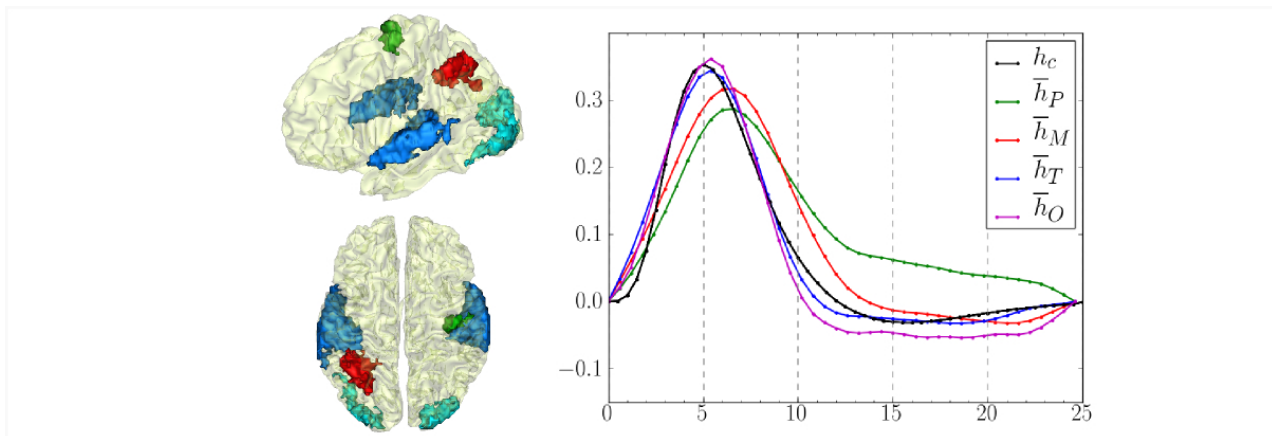


Figure 8. Left: Definition of regions of interest to investigate hemodynamics variability from JDE-based group-level analysis. Top: Sagittal view. Bottom: axial/top view. Left parietal area (P) appears in red, left motor area in the pre-central cortex is shown in green, Bilateral temporal regions along auditory cortices and bilateral occipital regions in the visual cortices are shown in blue and cyan, respectively. Right: Group-average HRF estimates for the four regions of interest: \bar{h}_P , \bar{h}_M , \bar{h}_T , \bar{h}_O stand for HRF means in parietal, motor, temporal and occipital regions, respectively. h_c correspond to the canonical HRF.

473 is supposed given a priori in the current JDE approach. The so-called joint Parcellation-Detection-
 474 Estimation (JPDE) validation is still ongoing. In an attempt to solve the same issue, an alternative based
 475 on random parcellations and consensus clustering has been recently proposed in **Badillo et al. (2013a)**.

476 Closely related to the results presented in Section 4.4, a multi-subject extension of the JDE is currently
 477 developed to properly account for the between-subject HRF variability and recover a meaningful and
 478 potentially less biased group-level HRF profile. This development trail will bring modification in the core
 479 design of `pyhrf` so as to take into account the new “group” data axis.

480 Finally, recent works have opened the path to multi-modality by the processing of Arterial Spin Labeling
 481 fMRI data **Vincent et al. (2013)**. To analyze such data, physiologically-inspired models are investigated to
 482 establish parsimonious and tractable versions of physiological models such as the balloon model described
 483 in **Friston and Buechel (2000)**; **Buxton et al. (2004)**. Hence, for validation purpose, the artificial data
 484 generator is also being enriched with the simulation of physiological models.

5.2 PACKAGE PERSPECTIVES

485 In addition to improving the documentation and usability of the current package version, additional
 486 developments will be first motivated by the above-mentioned methodological perspectives, namely re-
 487 factoring part of the data design to integrate the group-level and multi-session data components. This will
 488 mainly involve the modification of the `FmriData` class and the addition of a new `FmriGroupData`
 489 class. The handling of data input will have to be extended to exploit a hierarchy of subject-specific files.

490 We also plan to enrich the parcellation component by handling classical atlases such as the
 491 Automated Anatomical Labeling (AAL) atlas built by **Tzourio-Mazoyer et al. (2002)**, the Brodmann
 492 regions (**Brodmann (1909)**) and the Harvard-Oxford atlas (**Desikan et al. (2006)**) available in `FSL`¹⁸.
 493 The goal is to enable the definition of functional parcels that are consistent with previous studies in the
 494 literature and also to further investigate the anatomo-functional link by comparing atlas-driven versus
 495 data-driven parcellations.

496 In order to offer more user-friendliness, the building of a unified graphical user interface is foreseen,
 497 which will gather the XML editor and the viewer while also enabling the selection of the analysis

¹⁸ <http://http://fsl.fmrib.ox.ac.uk>

498 type. We also envisage resorting to wizard interfaces to guide the setup process and deliver contextual
499 documentation. In terms of browsing features, tools to properly explore the surface-based results are
500 currently missing, as we resort to an external tool, *anatomist*. The goal is not to reproduce all the
501 features offered by the latter which enable the output of paper-ready figures through joint volume/surface
502 rendering, data fusion and material handling. We rather think of a simple textured mesh viewer associated
503 with a picking feature in order to synchronize other views. The main usage is to make the selection of
504 a mesh node and the corresponding HRF estimate feasible. For making this surface-based rendering av-
505 available, *mayavi*¹⁹ is an appealing candidate since it has been already intensively used in the python
506 community.

507 Finally, we plan on incorporating GPU parallel computing features. This technology is becoming more
508 and more available and powerful and may also appear cheaper than CPU computing systems (see **Owens**
509 **et al.** (2008) for a review). Specifically, the NVIDIA chipsets are easily accessible for general
510 purpose computing through the python package *pyCUDA*²⁰. A simple test on matrix products with a
511 complexity similar to that of our models showed a gain of one order of magnitude in favor of GPU
512 computations²¹ (NVIDIA GeForce 435M graphics card) compared to CPU-based computations (Intel
513 Core M480 @ 2.67GHz) with *numpy*.

6 CONCLUSION

514 The *pyhrf* package provides tools to detect evoked brain activity and estimate the underlying dynamics
515 from fMRI data in the context of event-related designs. Several “reference” methods are available: the
516 GLM, FIR and RFIR approaches, and also more flexible models as provided by the JDE framework. The
517 choice of the analysis tools depends on the experimenter’s question: if simple mappings are required, the
518 GLM is appropriate provided that the HRF is expected to be close to its canonical version, but for finer
519 dynamics estimation, the JDE procedure is more suitable. The design of *pyhrf* allows the handling of
520 volumic and surfacic data formats and also the utilization of several distributed computing resources. The
521 main user interface is done by shell commands where the analysis setup is stored in an XML configuration
522 file. Two graphical components are provided: an XML editor and a n-dimensional volumic data browser.

523 This package provides valuable insights on the dynamics of the cognitive processes that are not available
524 in classical software such as SPM or FSL. Hence, it offers interesting perspectives to understand the
525 differences in the neuro-vascular coupling of different populations (infants, children, adults, patients,
526 etc.).

ACKNOWLEDGEMENT

527 The work of Philippe Ciuciu has been partially supported by the CIMI (Centre International de
528 Mathématiques et d’Informatique) Excellence program during winter and spring 2013.

REFERENCES

529 Andreev, K. and Räcke, H. (2004), Balanced graph partitioning, in Proceedings of the sixteenth annual
530 ACM symposium on Parallelism in algorithms and architectures (ACM, New York, NY, USA), SPAA
531 ’04, 120–124

¹⁹ <http://code.enthought.com/projects/mayavi/>

²⁰ <http://developer.nvidia.com/pycuda>

²¹ benchmark available at <http://wiki.tiker.net/PyCuda/examples/DemoMetaMatrixmulCheetah>

- 532 Aurenhammer, F. and Klein, R. (2000), Voronoi Diagrams. (Elsevier Science Publishing), chapter 5,
533 201–290
- 534 Badillo, S., Varoquaux, G., and Ciuciu, P. (2013a), Hemodynamic estimation based on consensus
535 clustering, in IEEE Pattern Recognition in Neuroimaging (PRNI) (Philadelphia, USA)
- 536 Badillo, S., Vincent, T., and Ciuciu, P. (2013b), Group-level impacts of within- and between-subject
537 hemodynamic variability in fMRI, *Neuroimage*, 82, 433–448
- 538 Badillo, S., Vincent, T., and Ciuciu, P. (2013c), Multi-session extension of the joint-detection framework
539 in fMRI, in 10th International Symposium on Biomedical Imaging (San Francisco, CA), 1504–1507
- 540 Bakhous, C., Forbes, F., Vincent, T., Dojat, M., and Ciuciu, P. (2013), Variational variable selection to
541 assess experimental condition relevance in event-related fMRI, in 10th International Symposium on
542 Biomedical Imaging (San Francisco, CA), 1500–1503
- 543 Boynton, G. M., Engel, S. A., Glover, G. H., and Heeger, D. J. (1996), Linear systems analysis of
544 functional magnetic resonance imaging in human V1, *The Journal of Neuroscience*, 16, 13, 4207–4221
- 545 Brodmann, K. (1909), Vergleichende Lokalisationslehre der Grosshirnrinde (Barth, Leipzig)
- 546 Buxton, R. B., g, K. U., Dubowitz, D. J., and Liu, T. T. (2004), Modeling the hemodynamic response to
547 brain activation, *Neuroimage*, 23, Supplement 1, S220–S233
- 548 Calhoun, V. D., Stevens, M. C., Pearlson, G. D., and Kiehl, K. A. (2004), fMRI analysis with the general
549 linear model: removal of latency-induced amplitude bias by incorporation of hemodynamic derivative
550 terms, *NeuroImage*, 22, 1, 252 – 257
- 551 Chaari, L., Forbes, F., Vincent, T., and Ciuciu, P. (2012), Adaptive hemodynamic-informed parcellation of
552 fMRI data in a variational joint detection estimation framework, in 15th Proceedings MICCAI (Springer
553 Verlag, Nice, France), LNCS 7512, (Part III), 180–188
- 554 Chaari, L., Vincent, T., Forbes, F., Dojat, M., and Ciuciu, P. (2013), Fast joint detection-estimation
555 of evoked brain activity in event-related fMRI using a variational approach, *IEEE Transactions on*
556 *Medical Imaging*, 32, 5, 821–837
- 557 Ciuciu, P., Poline, J.-B., Marrelec, G., Idier, J., Pallier, C., and Benali, H. (2003), Unsupervised robust
558 non-parametric estimation of the hemodynamic response function for any fMRI experiment, *IEEE*
559 *Transactions on Medical Imaging*, 22, 10, 1235–1251
- 560 Desikan, R. S., Ségonne, F., Fischl, B., Quinn, B. T., Dickerson, B. C., Blacker, D., et al. (2006), An
561 automated labeling system for subdividing the human cerebral cortex on mri scans into gyral based
562 regions of interest., *Neuroimage*, 31, 3, 968–980
- 563 Duyn, J. and Koretsky, A. (2011), Novel frontiers in ultra-structural and molecular MRI of the brain, *Curr.*
564 *Opin. Neurol.*, 24, 4, 386–393
- 565 Elor, Y. and Bruckstein, A. M. (2009), Multi-a(ge)nt graph patrolling and partitioning, in Proceedings of
566 the 2009 IEEE/WIC/ACM International Joint Conference on Web Intelligence and Intelligent Agent
567 Technology - Volume 02 (IEEE Computer Society, Washington, DC, USA), WI-IAT '09, 52–57
- 568 Friston, K. (1998), Imaging neuroscience: Principles or maps?, *Proceedings of the National Academy of*
569 *Sciences of the United States of America*, 95, 796–802
- 570 Friston, K. and Buechel, C. (2000), Attentional modulation of effective connectivity from V2 to V5/MT
571 in humans, *Proceedings of the National Academy of Sciences of the United States of America*, 97, 13,
572 7591–7596
- 573 Friston, K., Holmes, A. P., Poline, J.-B., Grasby, P., Williams, S., Frackowiak, R., et al. (1995), Analysis
574 of fMRI time-series revisited, *Neuroimage*, 2, 45–53
- 575 Henson, R., Andersson, J., and Friston, K. (2000), Multivariate SPM application to basis function
576 characterisations of event-related fMRI responses, volume 11, 468
- 577 Koslow, S. H. and Huerta, M. F., eds. (2013), Neuroinformatics: An Overview of the Human Brain Project
578 (Psychology Press)
- 579 Laguitton, S., Rivire, D., Vincent, T., Fischer, C., Geffroy, D., Souedet, N., et al. (2011), Soma-
580 workflow: a unified and simple interface to parallel computing resources, in MICCAI Workshop on
581 High Performance and Distributed Computing for Medical Imaging (Toronto)
- 582 Liu, T., Frank, L., Wong, E. C., and Buxton, R. B. (2001), Detection power, estimation efficiency, and
583 predictability in event-related fMRI, *Neuroimage*, 13, 4, 759–773

- 584 Makni, S., Ciuciu, P., Idier, J., and Poline, J.-B. (2005), Joint detection-estimation of brain activity in
585 functional MRI: a multichannel deconvolution solution, *IEEE Transactions on Signal Processing*, 53,
586 9, 3488–3502
- 587 Makni, S., Idier, J., Vincent, T., Thirion, B., Dehaene-Lambertz, G., and Ciuciu, P. (2008), A fully
588 Bayesian approach to the parcel-based detection-estimation of brain activity in fMRI, *Neuroimage*, 41,
589 3, 941–969
- 590 Marrelec, G., Benali, H., Ciuciu, P., Plgrini-Issac, M., and Poline, J.-B. (2003), Robust Bayesian
591 estimation of the hemodynamic response function in event-related BOLD MRI using basic
592 physiological information, *Human Brain Mapping*, 19, 1, 1–17
- 593 Ogawa, S., Lee, T., Kay, A., and Tank, D. (1990), Brain magnetic resonance imaging with contrast
594 dependent on blood oxygenation, *Proceedings of the National Academy of Sciences of the United States*
595 *of America*, 87, 24, 9868–9872
- 596 Operto, G., Bulot, R., Anton, J.-L., and Coulon, O. (2006), Anatomically informed convolution kernels
597 for the projection of fMRI data on the cortical surface, in Proceedings 9th International Conference
598 on Medical Image Computing and Computer Assisted Intervention (Springer Verlag, Copenhagen,
599 Denmark), LNCS 4191, 300–307
- 600 Owens, J., Houston, M., Luebke, D., Green, S., Stone, J., and Phillips, J. (2008), Gpu computing,
601 *Proceedings of the IEEE*, 96, 5, 879–899
- 602 Pinel, P., Thirion, B., Mriaux, S., Jobert, A., Serres, J., Le Bihan, D., et al. (2007), Fast reproducible
603 identification and large-scale databasing of individual functional cognitive networks, *BMC Neurosci.*,
604 8, 1, 91
- 605 Risser, L., Vincent, T., Forbes, F., Idier, J., and Ciuciu, P. (2011), Min-max extrapolation scheme for fast
606 estimation of 3D Potts field partition functions. application to the joint detection-estimation of brain
607 activity in fMRI., *Journal of Signal Processing Systems*, 65, 3, 325–338
- 608 Thyreau, B., Thirion, B., Flandin, G., and Poline, J.-B. (2006), Anatomico-functional description of the
609 brain: a probabilistic approach, in Proceedings 31th Proceedings of the International Conference on
610 Acoustic, Speech and Signal Processing, volume V (Toulouse, France), volume V, 1109–1112
- 611 Tzourio-Mazoyer, N., Landeau, B., Papathanassiou, D., Crivello, F., Etard, O., Delcroix, N., et al. (2002),
612 Automated anatomical labeling of activations in SPM using a macroscopic anatomical parcellation of
613 the MNI MRI single-subject brain., *Neuroimage*, 15, 1, 273–89
- 614 Vincent, T., Ciuciu, P., and Thirion, B. (2008), Sensitivity analysis of parcellation in the joint detection-
615 estimation of brain activity in fMRI, in 5th International Symposium on Biomedical Imaging (Paris,
616 France), 568–571
- 617 Vincent, T., Risser, L., and Ciuciu, P. (2010), Spatially adaptive mixture modeling for analysis of within-
618 subject fMRI time series, *IEEE Transactions on Medical Imaging*, 29, 4, 1059–1074
- 619 Vincent, T., Warnking, J., Villien, M., Krainik, A., Ciuciu, P., and Forbes, F. (2013), Bayesian Joint
620 Detection-Estimation of cerebral vasoreactivity from ASL fMRI data, in 16th Proceedings Proc.
621 MICCAI, LNCS Springer Verlag, volume 2 (Nagoya, Japan), volume 2, 616–623
- 622 Yan, L., Zhuo, Y., Ye, Y., Xie, S. X., An, J., Aguirre, G. K., et al. (2009), Physiological origin of low-
623 frequency drift in blood oxygen level dependent (bold) functional magnetic resonance imaging (fMRI),
624 *Magnetic Resonance in Medicine*, 61, 4, 819–827